

Electrometry of extremely-low frequencies from kHz to sub-Hz with a Rydberg-atom sensor

Aveek Chandra^{1,2*}, Narongrit Paensin³, and Rainer Dumke^{1,2,4}

¹*Centre for Quantum Technologies, National University of Singapore, 3 Science Drive 2, Singapore 117543*

²*School of Physical and Mathematical Sciences, Nanyang Technological University, 21 Nanyang Link, Singapore 637371*

³*Department of physics and Materials Science, Chiang Mai University, Chiang Mai, 50200, Thailand and*

⁴*Quantum Sensing Centre, 2 Science Park Drive, Singapore 118222*

(Dated: March 17, 2026)

Rydberg-atom electric field sensing has shown great potential from near-DC to THz with state-of-the-art measurement metrics realized in sensitivity, phase extraction, multi-band receptivity, etc. While Rydberg-atom sensors have shown exceptional performance in the GHz regime, low-frequency operation has remained challenging because of electric-field-screening in conventional vapor cells, which suppresses externally applied fields. We overcome this limitation by combining auxiliary modulation and lock-in detection with a paraffin coated vapor cell, and demonstrate an electrode-free, wideband method for sensing frequencies, ranging from 0.5 Hz to 10 kHz. Our work extends Rydberg-atom sensor's range to VLF, ULF, SLF, ELF and sub-ELF frequency bands. In our method, high state-of-the-art sensitivities have been achieved - $819 \mu\text{V}/\text{cm}/\sqrt{\text{Hz}}$ for 1 Hz, $33 \mu\text{V}/\text{cm}/\sqrt{\text{Hz}}$ for 10 Hz, $10 \mu\text{V}/\text{cm}/\sqrt{\text{Hz}}$ for 100 Hz and $2 \mu\text{V}/\text{cm}/\sqrt{\text{Hz}}$ for 1 kHz.

Atomic sensors are central to modern science and technology because atoms of a given species are identical, defect-free, and ultrasensitive to environmental changes. Rydberg atoms, with large DC polarizability and microwave-transition dipole moments, can efficiently measure electric fields over a broad frequency range. However, most demonstrations so far, including those achieving state-of-the-art sensitivities [1, 2] and continuous-band detection capabilities [3], have been in the GHz regime, where most conventional wireless communication and sensing occur. Low-frequency electric-field sensing and communication remain valuable for unique applications.

Low-frequency signals are highly penetrating and therefore important for long-range communication, as these wavelengths can propagate over long distances without attenuation, interference, or signal loss. Conventional low-frequency receivers, however, are bulky and noise limited because antenna size scales inversely with detection frequency, as given by the Chu limit [4]. Thus, antennas are typically meter-scale at MHz frequencies and several kilometers at kHz frequencies, making them impractical or unrealizable. Developing low-frequency quantum sensors or receivers that outperform classical receivers is therefore important.

Frequencies in the kHz range are used for underwater-to-air communication because they can penetrate seawater [7]. Low frequencies also enable tracking and localization of buried subsea cables [8], and noninvasive testing and characterization of electronic devices and industrial units, as shown for lithium-ion batteries [9]. Other applications include studies of electric-field pulsations below 1 Hz and turbulence in atmospheric science [10], low-frequency radio astronomy [11], and electromagnetic fields in geophysical [12] and biological [13] systems.

A Rydberg-atom sensor is typically a few centimeters long and can detect electric fields with high accuracy and sensitivity from near-DC to THz frequencies. This wideband capability makes it a practical, field-deployable receiver for RF signals across multiple bands in classical wireless communication and sensing [5]. For example, radar remote sensing of Earth's ecosystem, climate, and surface requires detection

across multiple bands in different frequency domains. Conventionally, this requires several receivers and electronic systems, each optimized for only a narrow frequency window. A Rydberg-atom sensor could instead receive multiple bands at different frequencies, shrinking and simplifying cumbersome multi-receiver architectures. Remote sensing of soil moisture with a Rydberg-atom sensor has been demonstrated in Ref. [6].

Low-frequency electric-field sensing is challenging because standard uncoated vapor cells screen DC and low-frequency fields. Although most alkali-metal atoms remain in the gas phase, a fraction adsorbs on the inner SiO₂ glass surface, forming a thin metallic layer that makes the surface conductive. When a DC or low-frequency field is applied, free charges in this layer redistribute to generate an opposing field that cancels the applied field. In steady state, the net field inside the cell is therefore zero, so the vapor cell behaves as a 'Faraday cage' for DC and low-frequency fields, making their detection impossible. Ref. [14] demonstrated low-frequency detection $\lesssim 1$ kHz with a sapphire vapor cell, but sensing was limited by a high spectral noise floor. Other studies [15–17] achieved low-frequency electric-field detection down to about a hundred hertz by inserting metal electrodes into the vapor cell, but this complicates the sensor design and can reduce sensitivity and performance.

In this paper, we demonstrate an electrode-free method of sensing extremely-low frequency electric fields ranging from 0.5 Hz to 30 kHz, covering sub-ELF, ELF, SLF, ULF and VLF frequency bands. The sensing of all frequencies under same operating condition, underlines the wideband sensing capability. By using a paraffin-coated cell, an auxiliary modulation field and lock-in detection technique, high sensitivities have been measured as reported in Table I.

The experimental schematic and the relevant energy levels of a Cs atom are presented in Fig. 1(a) and (b) respectively. We have used a spherical paraffin-coated vapor cell (pyrex) at room temperature in the experiment, the relevant details of the cell can be found in Ref. [18]. A probe laser at 852 nm, out-coupled from a polarization-maintaining fiber, is collimated and split into two beams - a probe beam with waist

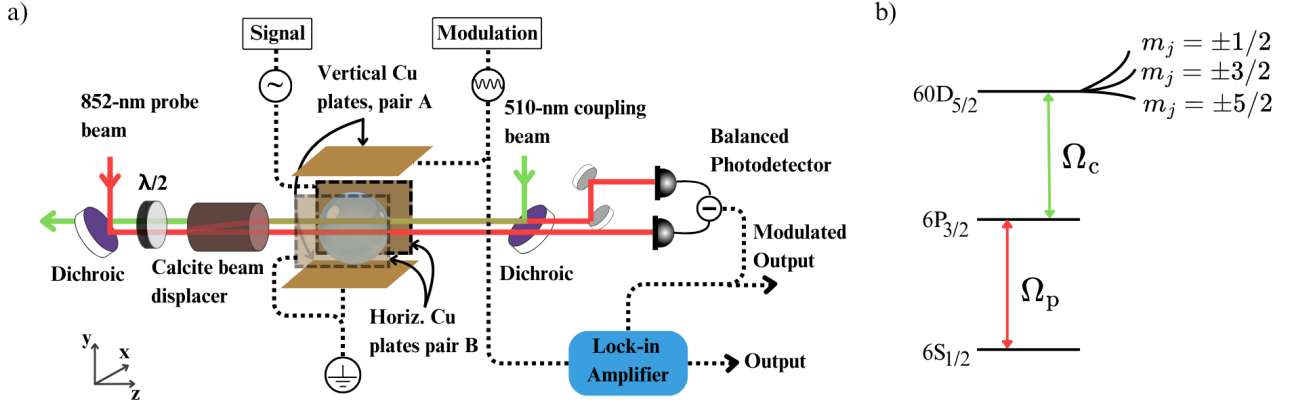


FIG. 1. a) Experimental setup. Probe (852 nm) and coupling (510 nm) beams with effective Rabi frequencies Ω_p and Ω_c overlap in a paraffin-coated vapor cell to create two-photon Rydberg excitations to $60D_{5/2}$. A balanced photodetector measures the transmission difference between the probe and an identical reference beam. Auxiliary modulation and signal fields are applied via copper plate pairs, and the lock-in amplifier provides a filtered, demodulated high-SNR output. b) Energy-level diagram for excitation to $60D_{5/2}$. In an electric field, the state splits into m_j sub-levels.

TABLE I. Measured sensitivities at various frequencies in this work.

Frequency (Hz)	Sensitivity ($\mu\text{V}/\text{cm}/\sqrt{\text{Hz}}$)
0.5	2636
1	819
2	395
5	82
10	33
20	17
100	10
200	5
1000	2
10000	5

0.26 mm and an identical reference beam. They propagate in parallel through the cell and finally collected on a balanced photodetector (PD) where the probe signal is subtracted from that of reference to obtain the transmission signal. A coupling laser at 510 nm, out-coupled from a polarization-maintaining fiber, is collimated to a beam waist of 0.45 mm. It counter-propagates and overlaps with the probe beam inside the vapor cell. Both probe and coupling beams have collinear polarization along the y -axis. The probe laser drives the D2 transition of Cs represented as $6|S_{1/2}\rangle \rightarrow 6|P_{3/2}\rangle$ with effective Rabi frequency $\Omega_p = 2\pi \times 29.5$ MHz (optical power $\sim 200\mu\text{W}$). The coupling laser drives the Rydberg excitation to $n = 60$ represented as $6|P_{3/2}\rangle \rightarrow 60|D_{5/2}\rangle$ with effective Rabi frequency $\Omega_c = 2\pi \times 1.7$ MHz (optical power ~ 42 mW).

Under two-photon resonance, Rydberg-EIT transparency peak appears in the transmission signal when the probe frequency is scanned over resonance. A balanced detection mode is used to remove the Doppler-broadened absorption background, and also to cancel out any intensity noise of the probe laser. In the experiment, both probe and coupling lasers are frequency-locked to a reference cavity - a dual-axis, cubic, ultra-low expansion (ULE) cavity, with very high-finesse. The details on the setup and laser-locking methods can be found in

S1 in Ref. [19].

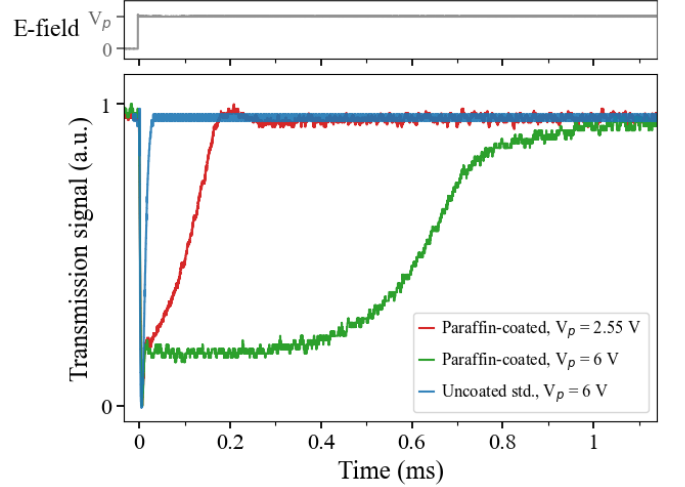


FIG. 2. Transient response induced by electric-field-screening in vapor cells. At $t = 0$, when DC bias field of amplitude V_p is switched on, the on-resonant transmission signal rapidly drops to zero as the resonant condition changes causing the Rydberg-EIT transmission peak to be frequency-shifted. Now, due to screening effect the field inside the vapor cell is slowly reduced to zero over some characteristic time (time constant, τ), shifting the Rydberg-EIT peak back to its original resonant frequency. For standard (uncoated) cell, $\tau = 10 \mu\text{s}$ is independent of the magnitude of V_p . For paraffin-coated cell, $\tau = 0.1$ (0.6) ms for $V_p = 2.55$ (6) V, which in terms of field amplitude = 354 (833) mV/cm.

Rydberg states experience quadratic energy (Stark) shift (Δf), in the presence of electric field (E). This is given by:

$$\Delta f = -\frac{\alpha}{2}E^2 \quad (1)$$

where α is the DC polarizability of the Rydberg state. Fig. 3(a) shows the energy shift experienced by Rydberg state

$60D_{5/2}$ when DC electric field is applied. With increase in electric field strength, the degeneracy in m_j sublevels is lifted that results in splitting and m_j dependent Stark shifts. The calculated polarizabilities (using ARC Rydberg calculator [20]) of the sublevels $m_j = \pm 1/2, \pm 3/2, \pm 5/2$ are $-4985 \text{ MHz cm}^2/\text{V}^2$, $-3624 \text{ MHz cm}^2/\text{V}^2$, $281 \text{ MHz cm}^2/\text{V}^2$ respectively.

In the experiment, the electric fields are applied to the paraffin-coated cell, via pairs of copper plates, A in vertical and B in horizontal direction as shown in Fig. 1(a). The plates have dimensions of a square of length 70 mm and thickness of 2 mm. The vertical plates (pair A) are separated by 72 mm while horizontal plates (pair B) are apart by 76 mm. The paraffin-coated, spherical vapor cell with a radius of 15 mm, is placed at the center in between the pairs of plates such that the electric field is uniform across the dimension of the cell.

At first, we study the effect of electric-field-screening in paraffin-coated cell relative to an uncoated (standard) cell. With both probe and coupling lasers frequency-locked to the reference cavity, we record the transmission signal at two-photon resonance. The transient responses for the standard (uncoated) cell and the paraffin-coated cell under the application of E-field with amplitude of 833 mV/cm is shown in Fig. 2. When the E-field is turned on at time $t = 0$, transmission signal rapidly drops to zero. This is because the two-photon resonance condition changes causing the Rydberg-EIT transmission peak to be shifted in frequency. In fact, the rate of decay of transmission signal is given by the bandwidth of the balanced photodetector. Now, due to the screening-effect from the free-surface charges, the E-field inside the vapor cell is slowly reduced to zero over some characteristic time, shifting the Rydberg-EIT peak back to its original resonant frequency. The characteristic time called screening-time constant τ , in our case is defined as the time over which the signal recovers to 0.5 of its initial value.

For standard (uncoated) cell, the transient signal (in blue) rapidly recovers, following an exponential profile, to its original value, $\tau = 10 \mu\text{s}$. However, for paraffin-coated cell, the transient signal recovers at a slower rate, and the rate even depends on the applied field amplitude. $\tau = 0.1$ (0.6) ms for $V_p = 2.55$ (6) V, which in terms of field amplitude is 354 (833) mV/cm. The different screening times for uncoated and paraffin-coated cells have been qualitatively explained in S2 in Ref. [19].

To move beyond acquisition on two-photon resonance and identify an optimal operating point P , we study the transmission signal at different probe detunings under an applied E-field. In the experiment, the probe detuning is varied with a fibered acousto-optic frequency shifter. The transient recorded at each detuning is compiled into the 2D color map shown in Fig. 3(b). Figure 3(a) shows the calculated Stark spectrum of the $60D_{5/2}$ state, which splits into its m_j branches as the field amplitude increases. Since each branch has a different DC polarizability, the operating point matters. The point ‘ P ’ corresponds to an applied field of 354 mV/cm. In the experiment, both the laser polarization and the applied field are along the vertical y direction, so most atoms populate the $m_j = \pm 1/2, \pm 3/2$ branches, as seen in Fig. 3(b). The

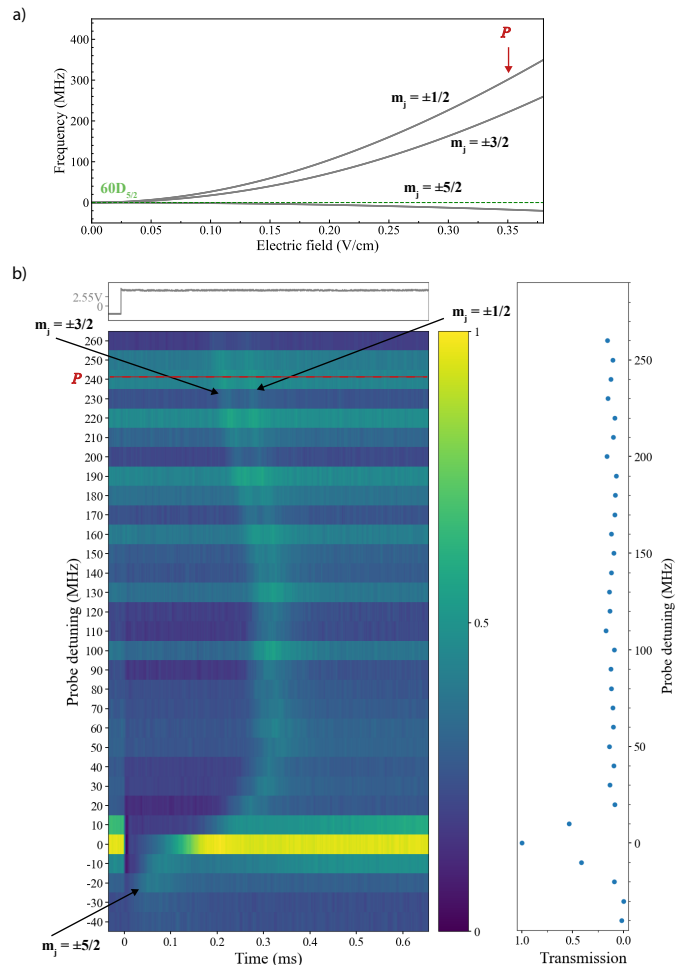


FIG. 3. (a) Calculated Stark spectrum of the $60D_{5/2}$ state for fields from 0 to 380 mV/cm, showing the m_j -dependent Stark shift. (b) At $t = 0$, a DC bias field of amplitude 354 mV/cm ($V_p = 2.55$ V) is switched on and the transient response is recorded at different probe detunings in a paraffin-coated cell. The resulting 2D color map shows the three split branches corresponding to $m_j = \pm 5/2, \pm 3/2, \pm 1/2$, with most atoms in $\pm 3/2, \pm 1/2$. The red dashed line ‘ P ’ marks $\delta_p = 243$ MHz, used for sensor operation. Right: Rydberg-EIT spectrum in the absence of electric field.

red dashed line marked ‘ P ’ corresponds to a probe detuning of $\delta_p = 243$ MHz, used later for sensor operation.

In summary, the slow electric-field-screening in paraffin-coated cells opens a time window during which the atoms are not yet shielded by the cell and are therefore available for sensing external electric fields.

First, direct sensing of low-frequency electric fields, without an auxiliary field, was performed. The field was applied to the atoms via a pair of copper plates, and sensing was demonstrated only for frequencies ≥ 500 Hz and amplitudes ≥ 100 mV/cm; see S4 in Ref. [19].

A sensor’s sensitivity is proportional to the slope of its response curve at the operating point P . Here, the response is the Stark shift (see Eq. 1) of the state m_j , with polarizability

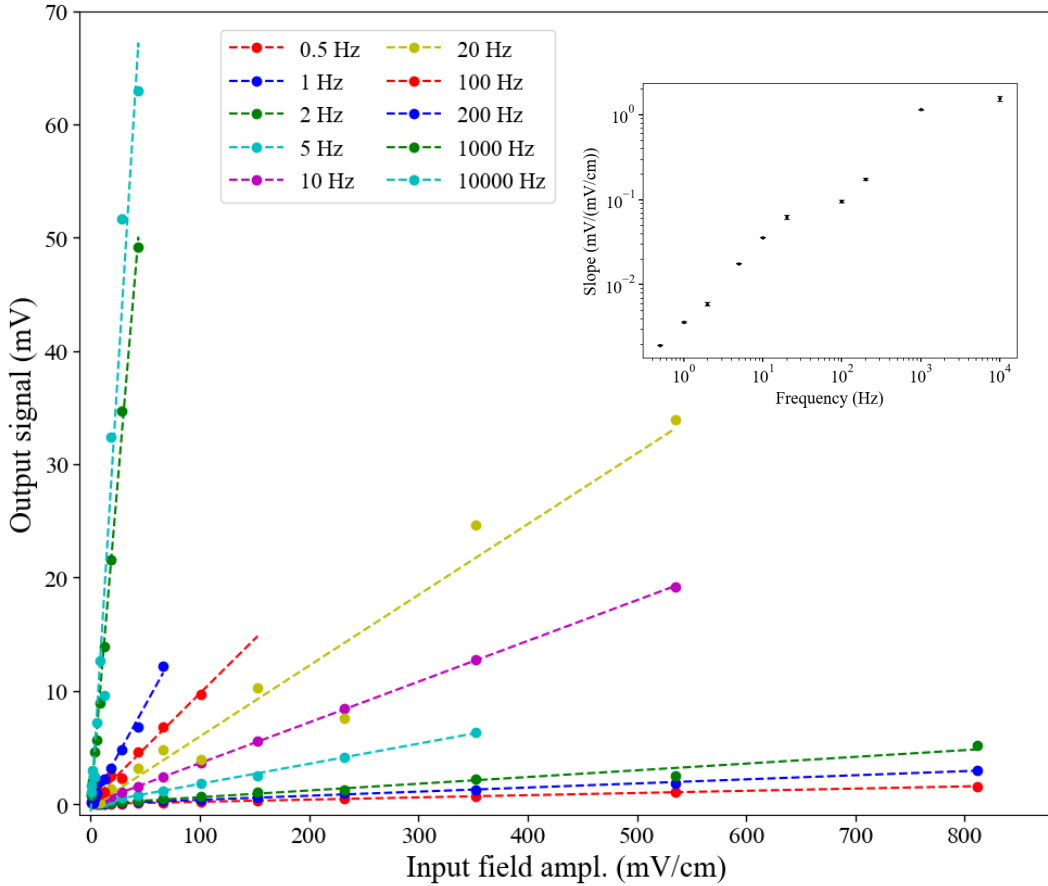


FIG. 4. Output signal versus input field amplitude in the linear regime for different low frequencies. Each dashed line is a linear fit to the data for the sensed frequency. Inset: slope $m(f)$ from the linear fit, plotted versus signal frequency, giving the sensor responsivity.

α_j , under an electric field of amplitude E :

$$\text{Sensitivity} \propto |d\Delta f/dE|_P = \alpha_j E \quad (2)$$

Sensitivity is therefore enhanced by operating at a point P with a steep slope, which requires both a larger field amplitude and an energy level with high polarizability. In our method, this is achieved with an auxiliary modulation field that brings the sensor to the operating point P , marked in Fig. 3(a) and Fig. 3(b). We choose P because the $m_j = \pm 1/2, \pm 3/2$ branches have higher polarizabilities than the $m_j = \pm 5/2$ branch, which has the lowest polarizability. The auxiliary field is applied via the vertical copper plate pair A shown in Fig. 1(a).

The auxiliary-field amplitude E_{aux} and corresponding probe detuning δ_p are chosen according to the intended operating domain. A larger E_{aux} requires a larger positive detuning δ_p to measure extremely low-amplitude fields (high-sensitivity domain), whereas a smaller E_{aux} requires detuning closer to two-photon resonance to measure relatively high-amplitude fields (low-sensitivity domain). Operating in both domains can therefore provide a large linear dynamic range. In this work, we focus on the former, high-sensitivity domain and choose $E_{\text{aux}} = 354$ mV/cm and $\delta_p = 243$ MHz after careful

optimization of the experimental parameters (details in S3 in Ref. [19]).

The modulation frequency f_{mod} is chosen so that the polarity of the auxiliary field flips when electric-field-screening begins to affect the atoms inside the cell. From Fig. 3(b), the $m_j = \pm 3/2, \pm 1/2$ branches cross the dashed line P at about 0.25 ms, corresponding to 4 kHz, which sets the lower limit on the modulation frequency. Its value is set empirically by maximizing the signal-to-noise ratio. For sensing frequencies from 0.5 Hz to 200 Hz, we use $f_{\text{mod}} = 7.9$ kHz. For 500 Hz and 1 kHz, $f_{\text{mod}} = 27.9$ kHz is used, while for 10 kHz, $f_{\text{mod}} = 87.9$ kHz is used.

In the experiment, the auxiliary modulation field E_{aux} and the signal field E_{sig} are applied to copper plate pairs A (vertical) and B (horizontal), respectively. The modulated output of the balanced photodetector (PD) is sent to one input of the lock-in amplifier (LIA), while the modulation field E_{aux} serves as the reference at the other input, as shown in Fig. 1. This enables synchronous demodulation at f_{mod} ; after appropriate filtering, the output provides the sensor signal. In the experiment, the low-pass filter cutoff is chosen as $1.265f$, where f is the frequency being sensed.

With the sensor operated at the point P , electric fields from 0.5 Hz to 10 kHz were detected, with both frequency and am-

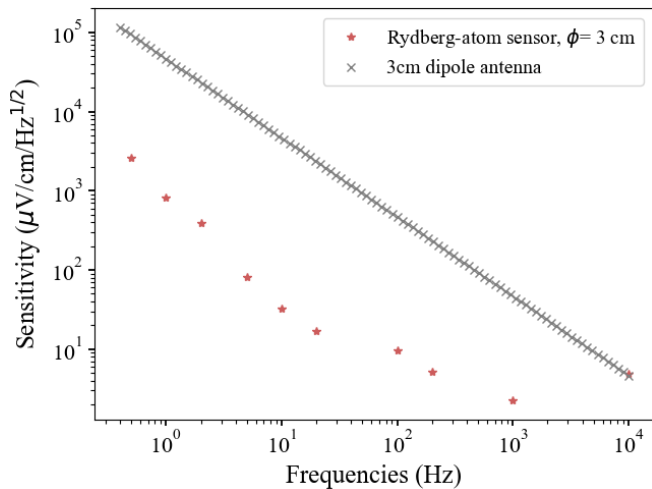


FIG. 5. Sensitivity of the Rydberg-atom sensor with vapor-cell diameter $\phi = 3$ cm (red), compared with the theoretically estimated field sensitivity of a classical receiver, a 3 cm dipole antenna (gray), at different frequencies. The Rydberg sensor shows about one to two orders of magnitude better sensitivity at extremely low frequencies. For frequencies $\gtrsim 1$ kHz, the two sensitivities begin to approach each other.

plitude measured for an input field of 43.7 mV/cm, as shown in Fig. S4 in Ref. [19]. The measurements were repeated over input amplitudes from 0.5 μ V/cm to 1 V/cm. The output begins to saturate as the input amplitude increases, and the saturation point depends on frequency. Figure 4 shows the measured output signal in the linear regime as a function of input amplitude for all frequencies. The slope $m(f)$ from the linear fit for each frequency, i.e. the sensor responsivity, is plotted versus signal frequency in the inset.

The variation of responsivity with signal frequency can be attributed to residual electric-field-screening. The auxiliary field at frequency f_{mod} does not eliminate screening completely, but mitigates it. As a result, the field experienced by the atoms before the auxiliary field switches is smaller than the applied, unscreened field. This residual screening therefore affects lower-frequency, longer-duration signals more strongly than higher-frequency, shorter-duration signals, accounting for the increase in responsivity $m(f)$ as the signal frequency rises from 0.5 Hz to 10 kHz.

The electric-field sensitivity at a given signal frequency can be estimated by identifying and characterizing the relevant noise sources in the experiment. The main contributors are laser intensity fluctuations and power drift, laser polarization drift, and noise from the balanced photodetector (PD) and lock-in amplifier (LIA). From Fig. 1(a), any polarization noise or drift is converted into intensity noise or drift.

Noise from the PD and laser intensity is measured together by recording the output of the balanced-PD with a spectrum analyzer (details in S6 in Ref. [19]). From this measurement, the relevant noise spectral density NSD_{PD} at the modulation frequency f_{mod} is obtained. The other contribution is the intrinsic noise of the LIA (see S6 in Ref. [19]), which is inevitably added to the demodulated output. This flicker noise

is intrinsic to the device and is specified by the LIA input voltage noise density NSD_{LIA} in the device manual. For uncorrelated noise sources, the total noise spectral density is $NSD_{total} = \sqrt{(NSD_{PD})^2 + (NSD_{LIA})^2}$.

Using the responsivity $m(f)$ discussed above, the field sensitivity at frequency f is estimated as $S_E = NSD_{total}/m(f)$.

The sensitivities achieved with the Rydberg-atom sensor using a vapor cell of diameter $\phi = 3$ cm are plotted in red in Fig. 5 as a function of signal frequency. For comparison, the theoretically estimated field sensitivity of a classical receiver of the same size, a 3 cm dipole antenna, is shown in gray [22]. The Rydberg-atom sensor is about one to two orders of magnitude more sensitive than the classical receiver at extremely low frequencies. For frequencies $\gtrsim 1$ kHz, the sensitivities of the classical and quantum sensors begin to approach each other.

Several techniques already implemented in the experiment lower the spectral noise floor. Frequency noise of the probe and coupling lasers, which is converted into intensity noise by the atomic spectroscopy, is mitigated by locking the laser frequencies to a high-finesse ULE cavity. Using a large probe detuning, $\delta_p = 243$ MHz, far from resonance, further reduces frequency-induced intensity noise. Finally, lock-in detection restricts the measurement to a narrow bandwidth and filters out broadband spectral noise. At present, probe-laser intensity fluctuations and power drifts primarily limit the sensor sensitivity. Ongoing noise-mitigation work is expected to improve it further.

Here, we demonstrate a wideband method for Rydberg-atom-based electric-field sensing from sub-Hz to a few kHz with state-of-the-art sensitivity. The achieved sensitivity is one to two orders of magnitude better than the theoretically estimated sensitivity of classical receivers of the same size at extremely low frequencies. For frequencies $\gtrsim 1$ kHz, the sensitivities of the classical and quantum sensors begin to approach each other. This method can be extended to higher frequencies, from hundreds of kHz to tens of MHz, provided a high-bandwidth balanced photodetector and a lock-in amplifier suitable for high-frequency demodulation are used. The sensor must also be operated at the optimal point P .

Paraffin-coated cells, widely used for all-optical magnetic-field sensing, are shown here to be excellent candidates for electric-field sensing, especially in the low-frequency domain. This opens the possibility of simultaneous, correlated sensing of electric and magnetic fields in biological specimens, novel materials, and geological studies. It may also open new frontiers in low-frequency radio astronomy and aid the search for exotic particles and fields via global sensor networks such as GNOME [21].

ACKNOWLEDGMENT

We would like to thank Alwaleed Aldhafeeri and Dr. Chee Wei Wong for sharing knowledge and insight on laser frequency stabilization. We also thank Dr. Michael Lim for helpful discussion.

The research has been supported by the National Research Foundation, Singapore and A*STAR under Quan-

tum Engineering Programme (NRF2021-QEP2-03-P01) as well as Centre for Quantum Technologies Funding Initiative (S24Q2d0009).

AUTHOR DECLARATIONS

The authors have no conflict of interest and no competing interests to declare.

The project was conceived and supervised by RD. AC performed the experiment with NP. AC contributed to the optimization, analysis and wrote the manuscript with inputs from RD. All the authors discussed the results and reviewed the manuscript.

Data availability

All data available from authors upon reasonable request.

* email: aveek.chandra@ntu.edu.sg

-
- [1] Wu, Bo *et al.*, Enhancing Sensitivity of Atomic Microwave Receivers Based on Optimal Laser Arrays. *IEEE Transactions on Antennas and Propagation* **73**, 2 (2025).
- [2] Tu, Hai-Tao *et al.*, Tony, Approaching the standard quantum limit of a Rydberg-atom microwave electrometer. *Sci. Adv.* **10**, 51 (2024).
- [3] Liu, Xiao Hong *et al.*, Continuous-Frequency Microwave Heterodyne Detection in an Atomic Vapor Cell. *Physical Review Applied* **18**, 5 (2022).
- [4] Chu, L. J., Physical Limitations of Omni-Directional Antennas. *Journal of Applied Physics* **19**, 12 (1948).
- [5] Gong, Tierui and Chandra, Aveek and Yuen, Chau and Liang Guan, Yong and Dumke, Rainer and Meng, Chong and See, Samson and Debbah, Mérouane and Hanzo, Lajos, Rydberg Atomic Quantum Receivers for Classical Wireless Communication and Sensing. *IEEE Wireless Communications* **22**, 12, 162-180 (2025).
- [6] Arumugam, D. *et al.*, Remote sensing of soil moisture using Rydberg atoms and satellite signals of opportunity. *Scientific Reports* **14** 18025 (2024).
- [7] Latypov, Damir, Compact quantum VLF/ELF sources for submarine to air communication. *2022 6th Underwater Communications and Networking Conference, UComms* (2022).
- [8] Szyrowski, T. *et al.*, Range extension for electromagnetic detection of subsea power and telecommunication cables. *Physical Review Applied* **21**, 2 (2019).
- [9] Barai, Anup *et al.*, A comparison of methodologies for the non-invasive characterisation of commercial Li-ion cells. *Progress in Energy and Combustion Science* **72**, 5, 1-31 (2019).
- [10] Anisimov, S. V. *et al.*, Universal spectra of electric field pulsations in the atmosphere. *Geophysical Research Letters* **29**, 24 (2002).
- [11] Bentum, M. J. *et al.*, A roadmap towards a space-based radio telescope for ultra-low frequency radio astronomy. *Advances in Space Research* **65**, 2 (2020).
- [12] Lei, Mingwei and Shi, Meng, Low-frequency electromagnetic fields in applied geophysics: Waves or diffusion? *GEO-PHYSICS* **71**, 4 (2006).
- [13] Tian, Haoyang *et al.*, System-level biological effects of extremely low-frequency electromagnetic fields: an in vivo experimental review. *Frontiers in Neuroscience* **17**, 10 (2023).
- [14] Jau, Yuan Yu and Carter, Tony, Vapor-Cell-Based Atomic Electrometry for Detection Frequencies below 1 kHz. *Physical Review Applied* **13**, 5 (2020).
- [15] Chen, M.*et al.*, Electric Field Manipulation of Rydberg States for Very Low Frequency Fields Detection. arXiv:2501.08787 (2025).
- [16] Lei, Mingwei and Shi, Meng, High sensitivity measurement of ULF, VLF, and LF fields with a Rydberg-atom sensor. *Optics Letters* **49**, 19 (2024).
- [17] Li, Ling *et al.*, Super low-frequency electric field measurement based on Rydberg atoms. *Optics Express* **31**, 18 (2023).
- [18] Crepaz, H, Ley, L. Y. and Dumke, R. Cavity enhanced atomic magnetometry *Scientific Reports* **5**, 15448 (2015).
- [19] See Supplemental Material.
- [20] Sibalic, N., Pritchard, J.D., Adams, C.S., Weatherill K.J., ARC: An open-source library for calculating properties of alkali Rydberg atoms. *Computer Physics Communications* **220**, 319-331 (2017).
- [21] Afach, S. *et al.*, Characterization of the global network of optical magnetometers to search for exotic physics (GNOME). *Physics of the Dark Universe* **22**, 12, 162-180 (2018).
- [22] Meyer, D. H. *et al.*, Assessment of Rydberg atoms for wideband electric field sensing. *J. Phys. B: At. Mol. Opt. Phys.* **53**, 034001 (2020).

Supplementary Material

S1. LASER-FREQUENCY STABILIZATION SETUP

In atomic spectroscopy experiments, laser frequencies typically need to be locked to some frequency reference for achieving high-degree of frequency stability. In our case, this is provided by a cubic, dual-axis, ultra-low expansion (ULE) cavity placed in high vacuum environment. The ULE cavity (from Stable Laser Systems) has two axes, each with mirrors customized with respective high-reflectivity coatings at 510 nm and 852 nm. The specifications are: FSR = 3 GHz, finesse > 250000 for 852 nm axis and finesse = 50000 – 150000 for 510 nm axis. The full experimental schematic can be understood by combining Fig S1 and Fig 1 in the main text . A fibered probe laser at 852 nm is split into two outputs by a fibered splitter. One output is prepared into a free-space for Rydberg-atom sensing by out-coupling light from a polarization-maintaining fiber while the other output is sent to laser-frequency stabilization setup. In a similar manner, a fibered coupling laser at 510 nm is divided into two parts - one for Rydberg-atom sensing and the other for frequency stabilization.

Pound-Drever-Hall (PDH) scheme is implemented to lock the laser frequencies. The coupling beam is phase-modulated by a fibered-EOM (from Jenoptik) that creates frequency sidebands about a fixed frequency (typically a few MHz). The modulated beam with polarization appropriately aligned, is coupled into the ULE cavity. The beam coupled out of the cavity is detected by low-noise photodiode (PD) whose output signal is then demodulated to produce the error signal that is fed back, via servo-PID controller, to the laser. The fast feedback is sent to laser current while the slow feedback goes to laser piezo (PZT) system. For the coupling laser, we found empirically found a cavity-transmission peak occurring roughly at about the same frequency that is required for excitation to the Rydberg state $60D_{5/2}$.

For the probe laser, it is found that cavity-transmission peak is far off ($\gtrsim 1$ GHz) from the two-photon resonance frequency, hence offset-sideband locking is implemented. This allows the frequency of probe laser to be shifted as well as frequency stabilized. The laser frequency is shifted by a fibered-EOM with frequency offset sourced from signal generator 1, while the modulation-sidebands are generated about this offset frequency using external phase modulation sourced from signal generator 2. The rest of the frequency locking mechanisms are identical to that of the coupling beam. The probe frequency has been shifted in the experiment with fibered acousto-optic frequency shifter (AOM) in the probe beam path.

S2. SCREENING MECHANISM IN VAPOR CELLS

For standard (uncoated) cell, the adsorption of cesium atoms on the inner glass surface creates an effective ultra-thin metallic film with conductivity that is orders of magnitude

higher than the conductivity of glass. This allows rapid redistribution of surface-free charges similar to that of a metallic conductor giving an electric-field screening time $\tau = 10 \mu\text{s}$. The inner-surface sheet resistance is estimated to be $R_s \sim 30 \text{ M}\Omega$.

For paraffin-coated cell, there is an effective ‘metal-contaminated-paraffin’ thin film formed on the inner surface because of the adsorption of cesium atoms to the paraffin-wax layer on the inner surface of the cell. The alkali atoms effectively act as metallic dopants, creating localized states or percolation networks that allow the surface-free charges to be mobile on the thin-film paraffin coating, which otherwise is an insulator. However, the mobility of surface-free charges although non-zero is still significantly less compared to the free-charge mobility for the case of uncoated cell. Additionally, the free-charge mobility is found to be dependent on the applied field amplitude as the screening time is observed to increase from 0.1 ms to 0.6 ms when the field amplitude is changed from 354 mV/cm to 833 mV/cm.

S3. FINDING OPTIMAL OPERATING POINTS

The sensor operation depends largely on amplitude and frequency of auxiliary modulation field E_{aux} as well as probe detuning δ_p . A set of these 3 parameters define an operating point P, that are chosen after careful optimization. A signal field, E_{sig} of extremely low-frequency 10 Hz is chosen with amplitude of about 100 mV/cm. Now, the auxiliary modulation amplitude E_{aux} is scanned from 250 mV/cm to 500 mV/cm while the probe detuning δ_p is varied from 160 to 270 MHz initially with coarse-grained steps and finally with fine-grained steps. The demodulated output of LIA is recorded at each point and fitted with a sine function. The fitted sine amplitudes are plotted in a 2D color map, which helps to find an optimal operating point. A sample such dataset is shown in Fig.S2 with a smaller (zoomed-in) range of E_{aux} and δ_p . The ‘‘bright yellow’’ squares in 2D color map are points where the fitted output signal has maximum amplitude. Therefore, they represent optimal points that can be chosen for sensor operation. In our case, we have chosen $E_{\text{aux}} = 354 \text{ mV/cm}$, $\delta_p = 243 \text{ MHz}$, i.e. the square marked with ‘P’.

S4. DIRECT LOW-FREQUENCY SENSING

Here, the signal field is applied to the vertical pair of copper plates (could be applied to horizontal pair as well), without any auxiliary modulation field. The frequency to be sensed, appears as modulation on the transmission signal as Rydberg energy level is modulated by the Stark effect. Fig. S3 plots the signal-to-noise ratio (SNR) at the output for various frequencies input field of amplitude 100 mV/cm. As shown, frequencies below 500 Hz cannot be detected, and for frequencies $\geq 500 \text{ Hz}$, SNR improves with increase in signal

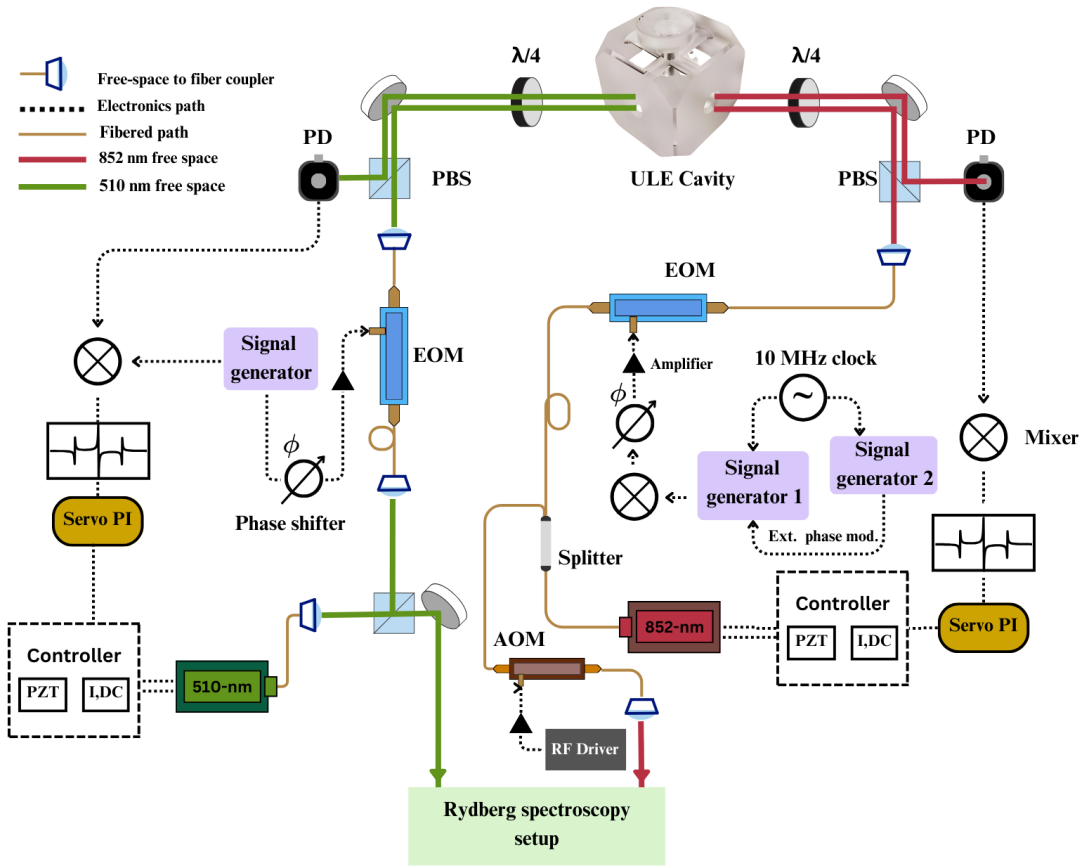


FIG. S1. Setup for frequency-stabilization and beam preparation. A fraction of probe and coupling lasers are sent to ULE cavity for frequency locking via PDH scheme. The rest of their power, after preparation, are sent to Rydberg spectroscopy setup for sensing.

frequency. To summarize, direct sensing of low-frequency fields with paraffin-coated cell, does not allow detection of extremely-low frequencies and for low frequencies that are

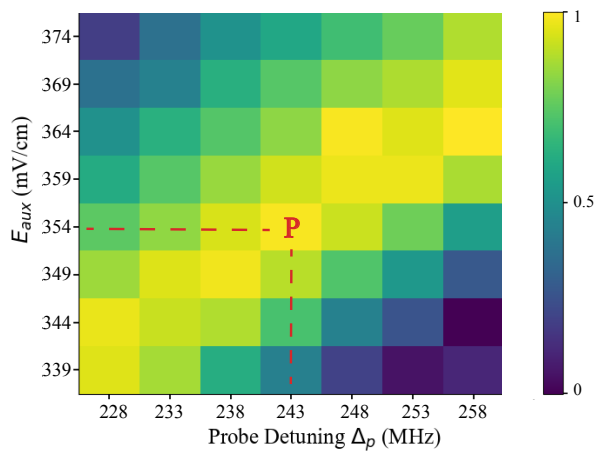


FIG. S2. 2D grid for a range of auxiliary field amplitudes E_{aux} and probe detunings δ_p . The color scale represents fitted sine amplitudes at the output for an input field of frequency 10 Hz and amplitude 100 mV/cm. The chosen operating point (square marked with 'P') is: $E_{\text{aux}} = 354$ mV/cm, $\delta_p = 243$ MHz.

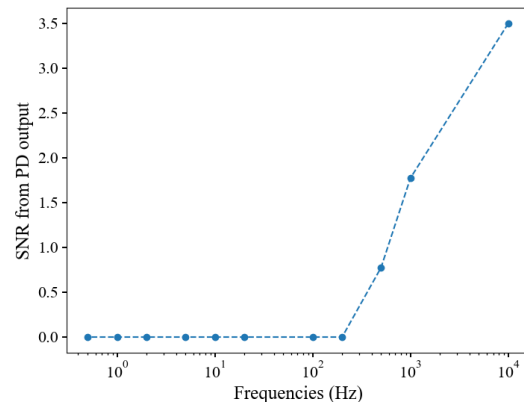


FIG. S3. Direct sensing of low frequencies ≥ 500 Hz with amplitude 100 mV/cm measured at $\delta_p = -7$ MHz, when E-field applied in vertical direction.

detected, the sensitivity is relatively poor by orders of magnitude when compared to sensitivity obtained from classical receivers.

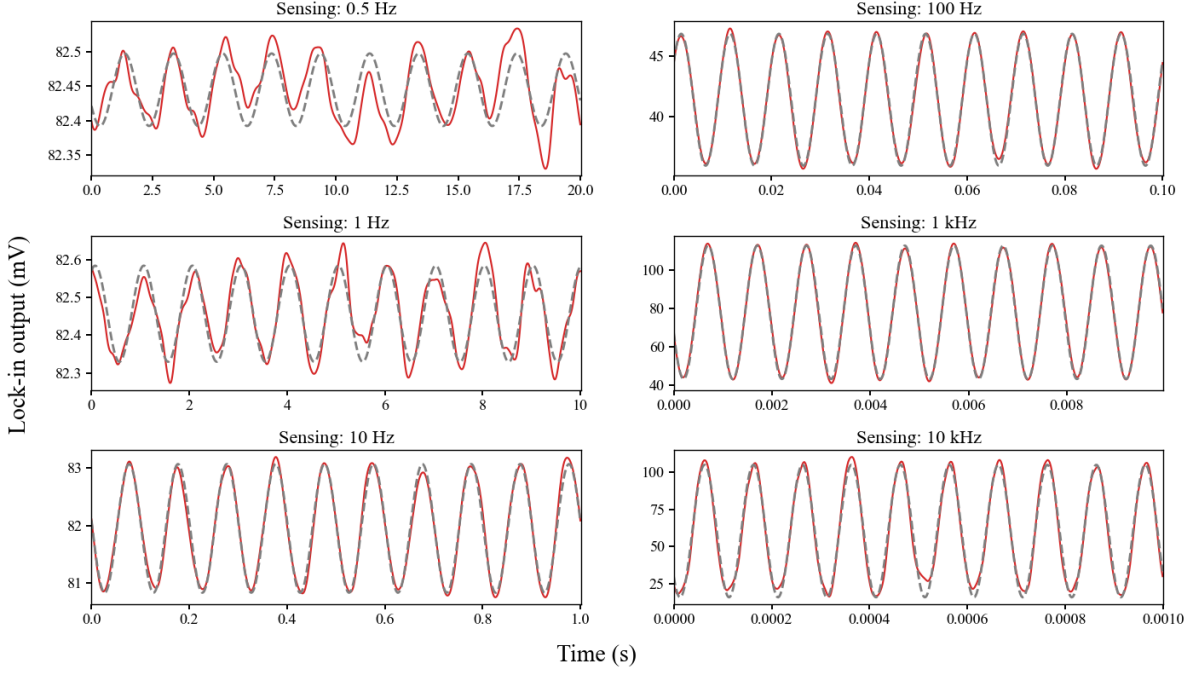


FIG. S4. Demodulated output of lock-in amplifier for frequencies - 0.5 Hz, 1 Hz, 10 Hz, 100 Hz, 1 kHz, 10 kHz with an input (applied) field of 43.7 mV/cm. The dashed lines (gray) are sinusoidal fits to the raw output.

S5. DEMODULATED OUTPUT SIGNALS

The demodulated raw output of LIA has been plotted in time domain in Fig. S4 for frequencies - 0.5 Hz, 1 Hz, 10 Hz, 100 Hz, 1 kHz, 10 kHz with an input (applied) field of 43.7 mV/cm. As seen, the output signals are easily fitted with sine function demonstrating a high signal-to-noise ratio typically achieved in our method. In a similar way, the fitting to the raw output signal has been performed for other values of input amplitudes and frequencies.

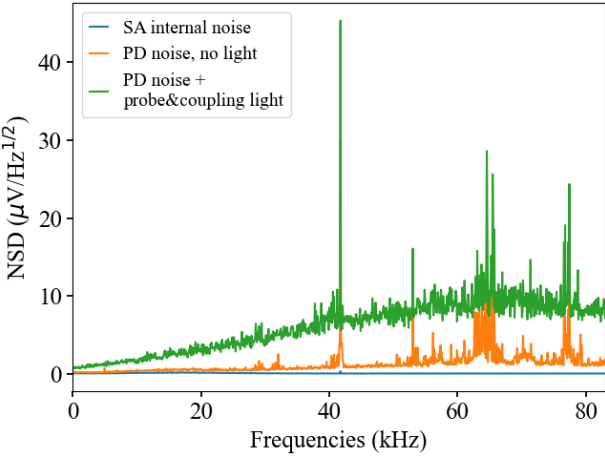


FIG. S5. Noise spectral density (NSD) as function of frequency measured with a spectrum analyzer (SA). SA background noise (blue), internal PD noise with no light (orange) and the laser intensity noise combined with PD noise (green) are shown here.

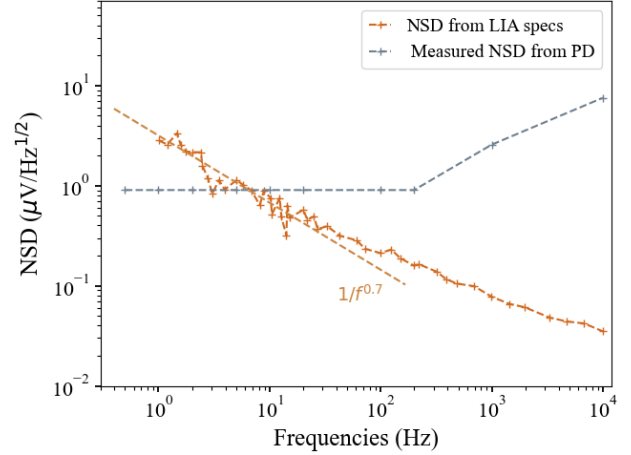


FIG. S6. Voltage noise density as function of signal frequency. The total noise density is square-rooted sum of noise densities from LIA (dark gray) and PD (brown).

S6. NOISE MEASUREMENT AND ANALYSIS

The key to estimation of field sensitivity is to finding out noise sources at a given frequency that fundamentally set the lower limit for detection of E-field amplitude in 1 Hz bandwidth. The impact of various noise sources in our experiment is studied here. The primary sources are - lock-in amplifier (LIA) and balanced photodetector (PD).

The balanced photodetector (PD) model is PDB450A from Thorlabs. It has been used with highest gain setting, i.e. trans-impedance gain, $G= 10^7$ V/A, bandwidth = 100 kHz. The total noise from PD is found by measuring the spectral content

of PD output via a spectrum analyzer (SA). Fig. S5 shows such a measurement where the power (dBm converted to μV) at each frequency is recorded with resolution bandwidth (RBW) of 1 Hz. SA background noise and internal PD noise (with no light) are shown by blue and orange traces. The green trace captures laser intensity noise combined with PD noise. It has been recorded when both lasers are frequency-locked and the sensor in operation (i.e. same probe detuning δ_p and Rabi frequencies Ω_p, Ω_c as used in operating point P). Due to lock-in detection, the noise density at modulation frequency f_{mod} is only relevant and the measured values $\text{NSD}_{\text{PD}} = 0.9, 2.57, 7.54 \mu\text{V}/\sqrt{\text{Hz}}$ for $f_{mod} = 7.9, 27.9, 87.9 \text{ kHz}$ effectively accounts for all noise originating from PD. They are represented by points (in gray) in Fig. S6.

The lock-in amplifier (LIA) model is MFLI 500 kHz from Zurich Instruments. Apart from the contribution originating from PD, the inherent noise generated by LIA also adds noise to its demodulated output. This is actually given by the input voltage noise density, that is provided by the device manual. It happens to be flicker noise and when fitted show $1/f^{0.7}$ dependency. Knowing this dependency helps us to find the noise density at 0.5 Hz which is not provided by the manual. The relevant values of NSD_{LIA} are indicated (in brown) in Fig. S6.

Now, the total noise spectral density is obtained by combining both spectral densities. Since noise sources are uncorrelated, the total noise spectral density is given by:

$$\text{NSD}_{\text{total}} = \sqrt{(\text{NSD}_{\text{PD}})^2 + (\text{NSD}_{\text{LIA}})^2}$$

Subsequently, the field sensitivity at signal frequency f is estimated from the relation

$$S_E = \text{NSD}/m(f)$$

where $m(f)$ is the slope obtained from linear fits to measured data as discussed in the main text.

For extremely-low frequencies close to DC, the noise floor is typically very high as it is dominated by flicker noise $1/f^\alpha$ where the exponent $0 < \alpha < 2$ depends on electronic systems (photodetector, ADC, DAC, etc.) under consideration. However in our case, the sensor is unaffected by this noise as lock-in detection technique allows measurements at the modulation frequency f_{mod} in a narrow bandwidth where the noise floor is dominated by the white noise of the PD. Therefore, the narrow detection bandwidth is given by the cutoff frequency (i.e. $1.265f$) of LIA low-pass filter, where f is the signal frequency.